Biosensors and Bioelectronics 120 (2018) 55–63

Contents lists available at ScienceDirect

Biosensors and Bioelectronics

journal homepage: www.elsevier.com/locate/bios

Layer-by-layer assembled gold nanoparticles/lower-generation (Gn ≤ 3) polyamidoamine dendrimers-grafted reduced graphene oxide nanohybrids with 3D fractal architecture for fast, ultra-trace, and label-free electrochemical gene nanobiosensors

Kumarasamy Jayakumar[a,d,e,*], María Belén Camarada[b], Rajendiran Rajesh[c], Rengarajan Venkatesan[c], Huangxian Ju[d], Venkataraman Dharuman[a,**], Yangping Wen[e,**]

[a] Department of Bioelectronics and Biosensors, Alagappa University, Karaikudi 630003, India
[b] Centro de Nanotecnología Aplicada, Facultad de Ciencias, Universidad Mayor, Santiago, Chile
[c] Department of Chemistry, Pondicherry University, Pondicherry 6050114, India
[d] State Key Laboratory of Analytical Chemistry for Life Science, Department of Chemistry, Nanjing University, Nanjing 210023, PR China
[e] Institute of Functional Materials and Agricultural Applied Chemistry, Jiangxi Agricultural University, Nanchang 330045, PR China

ARTICLE INFO

Keywords:
Electrochemical gene nanosensor
Reduced graphene oxide
Polyamidoamine dendrimer
Gold nanoparticle
Layer by layer assembly
Three-dimensional architecture

ABSTRACT

Three layer-by-layer (LBL) assembled gold nanoparticles (AuNPs)/lower-generation (Gn ≤ 3) polyamidoamine dendrimer (PD) with reduced graphene oxide (rGO) as the core/mercaptopropinoic acid (MPA)/Au were successfully fabricated and employed as electrochemical gene nanobiosensing platforms with three-dimensional (3D) fractal nanoarchitecture for fast, ultra-trace determination of label-free DNA hybridization. Three Gn ≤ 3PD were initially grafted to graphite oxide (GO) via the covalent functionalization between amino terminals of PD and carboxyl terminals of GO where a concomitant reduction of GO, which were covalently linked onto MPA that was self-assembled onto Au substrate, and finally AuNPs were encapsulated onto GG1PD by strong physicochemical interaction between AuNPs and -OH of rGO in GG1PD, Their morphologies, structures, electrochemical properties, and gene nanobiosensing performances were characterized and evaluated. AuNPs/GG2PD-based probe displayed the best excellent structural stability, lowest mobility on solid surface with the increasing charge resistance, widest linear range (1.1×10^{-6} – 1×10^{-18}), and the lowest limit of detection (1.87×10^{-19} M) in comparison with both AuNPs/GG1PD-based and AuNPs/GG3PD-based probes. This work will provide a new candidate for the development of metal nanoparticles functionalized PD with inorganic nonmetallic nanomaterials as cores with 3D fractal nanoarchitecture and promising electrochemical gene nanobiosensing platforms based on dendrimer-nanoinorganic hybrids with 3D nanoarchitectures and LBL assembly for fast and ultra-trace detection of label-free DNA hybridization with potential application in bioanalysis and medical diagnosis of genetic diseases.

1. Introduction

The ultra-trace and specific detection of nucleic acids is an extremely important tool in biological research such as bimolecular analysis, forensic investigations, genetic disease diagnostics, environmental and food safety monitoring. Many biochemical methods including rolling circle amplification, polymerase chain reaction, and nucleic acid sequence-based amplification have been reported for ultra-trace and specific detection of nucleic acids by the signal amplification of biochemical reactions. Other like fluorescence and chemiluminescence have also been developed. Biosensors as new bioanalytical tools with high specificity and low cost provide fast, reliable and sensitive measurements of DNA (Sang et al., 2016). These new biosensing techniques are also combined with traditional analytical methods together to detect DNA at ultralow levels (Liu et al., 2009). But they require a complicated and time-consuming operation, high cost, tedious labels and dedicated instruments. Electrochemical methods are new alternatives for the development of efficient DNA biosensors due to superior

* Corresponding author at: State Key Laboratory of Analytical Chemistry for Life Science, Department of Chemistry, Nanjing University, Nanjing 210023, PR China.
** Corresponding authors.
E-mail addresses: jkvare@gmail.com (K. Jayakumar), dharumanudhay@yahoo.com (V. Dharuman), wenyangping1980@jxau.edu.cn (Y. Wen).

https://doi.org/10.1016/j.bios.2018.08.032
Received 25 June 2018; Received in revised form 8 August 2018; Accepted 13 August 2018
Available online 16 August 2018
0956-5663/

features of simple and portable instruments, fast response, and low cost (Jayakumar et al., 2018a). Genosensors were designed to detect a specific DNA fragment by hybridization with complementary DNA fragment. Moreover, the label-free detection of gene does not require specific reagents. Electrochemical genosensors for the ultra-trace determination of label-free DNA hybridization with ultrahigh sensitivity, specific selectivity and fast analysis can be developed using a variety of nanomaterials and their three-dimensional (3D) nanoarchitectures as well as layer-by-layer (LBL) assembly (Lei and Ju, 2012).

Poly (amidoamine) dendrimers (PD) are very interesting commercially available macromolecules with well-defined 3D nanoscale hyperbranched polymeric architectures. ethylenediamine, ferrocene, zinc porphyrin, and polyethylene glycol as PD cores has been employed to regulate rigid structures of PD, which could enhance mobile charge carriers, increase active sites for the functionalization of biomolecules, and improve the electrochemical behaviours of PD (Trinchi and Muster, 2007). PD with various cores have been employed for the recent development of biosensors due to its controllable size and structure, modifiable surface functionalities, high mechanical and chemical stability, mono-dispersity, hydrophilicity. These properties make them extraordinary matrixes for the recognition and binding of biomolecules, the enhanced target capturing ability, excellent sensitivity, specificity, stability and reusability of biosensors (Trinchi and Muster, 2007; Bromfield et al., 2016). Furthermore, PD with highly dendritic structures can form more interaction sites between most of their branch ends and functionalized materials via multiple conjugations on the electrode surface (Trinchi and Muster, 2007; Rao Vusa et al., 2016; Rahman et al., 2000), and lesser diffusion limits are achieved through targets and electron transferring molecules due to internal spaces and reactive groups.

To date, the development of polymeric nanocomposites based on nanomaterials for applications in electronic and sensing fields attracted significant interest due to their high stability, conductivity and biocompatibility (Chen and Chatterjee, 2013; Chen et al., 2012; Guo and Wang, 2011). Nanomaterials as PD cores have more catalytic active sites because of high surface volume ratios, good structural stability, and excellent improvement of DNA biosensing via the increasing charge transfer properties. Carbon nanotubes as cores for the second generation (G2) PD have provided a unique nanostructure with low reaction times and cost effects that could increase the charge transfer resistance with the hybridization of target DNA and improve the sensitivity and selectivity of DNA biosensors (Li et al., 2015). Graphene oxide (GO), a two-dimensional carbon nanomaterial with a large surface area, has many oxygen functional groups such as hydroxyl, epoxide and carbonyl groups, which can be easily activated to functionalize PD. Unlike GO, the electrical conductivity of reduced graphene oxides (rGO) can be recovered by restoring the π network. More importantly, preparative methods for grafting organic or polymeric moieties onto rGO surface can retain the structural integrity of rGO framework in which there is no loss of electronic structure (Kumar et al., 2012), and covalent chemical modification of rGO had widespread concern and employed in different fields. We previously reported rGO as the core of the first generation (G1) PD for the development of highly-sensitive biosensing platform with controllable 3D nanoarchitecture and fast, trace differential pulse voltammetric analysis of label-free DNA hybridization (Jayakumar et al., 2018b).

Recent studies indicated metal nanoparticles (NPs) and dendrimers functionalized nanomaterials paved a way for improving the stability and electronic activity in biosensing fields, especially the combination of gold nanoparticles (AuNPs), dendrimers functionalized graphene or GO could enhance sensing performance (Trinchi and Muster, 2007; Bromfield et al., 2016; Chen and Chatterjee, 2013; Chen et al., 2012; Guo and Wang, 2011; Jayakumar et al., 2018b). AuNPs encapsulated PD have been widely investigated because of their potential applications in drug delivery agents, chemical sensors, nanoscale catalysts and light-harvesting antenna macromolecules (Kleinman et al., 2000). The interaction of metal NPs with PD are classified in three major categories (Rahman et al., 2000): (i) dendrimers encapsulated metal ions (Brunetti et al., 2015), (ii) metal ions as an integral part of dendrimers structure (Zhou et al., 2000), and (iii) dendrimers with peripheral groups that can bind metal ions. Organic chromophores have been attached to the periphery of metal modified PD to generate novel light-harvesting antenna systems (Aixue et al., 2007). Aixue et al. reported AuNPs-PD nanocomposites with high stability and enhanced electron charge transfer for the specific detection of DNA. More recently, only the functionalization of higher-generation (Gn > 3)PD with larger and circular structures can stabilize AuNPs via capping and the hydrophobic effect, which has been applied for DNA biosensing (Xu et al., 2017), but their lower-generation (Gn ≤ 3)PD for genosensors remain unexplored. Moreover, PD nanocomposites displayed the improvement of electrochemical properties and the enhanced performance of electrochemical DNA biosensors, but only Gn > 3PD have been tested (Bromfield et al., 2016; Rao Vusa et al., 2016; Trinchi and Muster, 2007; Rahman et al., 2000).

In this work, we report three LBL assembled AuNPs/Gn ≤ 3PD/mercaptopropinoic acid (MPA)/Au as electrochemical gene nanobiosensors with 3D fractal nanoarchitecture for fast, ultra-trace determination of label-free DNA hybridization. rGO was used as the Gn ≤ 3PD core via the covalent functionalization. AuNPs/GGn ≤ 3PD was obtained by the interaction between AuNPs and -OH groups of rGO in PD. New dendrimer-nanoinorganic hybrids were developed by the LBL assembly and the rGO functionalization.

2. Experimental sections

2.1. Materials and reagents

Details on suppliers for materials and reagents were given in Electronic Supplementary information (ESI).

2.2. Instruments

Details on suppliers for instruments were listed in ESI.

2.3. Synthesis of GGn ≤ 3PD

Details on syntheses of GGn ≤ 3PD were presented in ESI, and Scheme 1 gave the schematic procedure for syntheses of GGn ≤ 3PD.

2.4. Preparation of AuNPs/GGn ≤ 3PD electrodes

Details on preparation of AuNPs/GGn ≤ 3PD electrodes was demonstrated in ESI.

2.5. Detection of DNA hybridization

Details on detection of DNA hybridization were listed in ESI.

3. Results and discussion

3.1. Morphologies and microstructures of AuNPs/GGn ≤ 3PD

The rGO nanosheets exhibit a wrinkled and folded structure (Fig. 1a), but rGO functionalized with PD are a fairly smooth surface (Fig. 1b-d). It is confirmed that GGn ≤ 3PD has silk-like wrinkles, and restacking or folding layers are observed after the covalent modification with PD. HR-TEM images of Fig. 1c and d revealed a wrinkled and folded structure of GGn ≤ 3PD. The flattening and/or crumpling nanolayer with 3D nanostructure was also functionalized with 2 and 3 generation PD. Zhong et al. (Zhong et al., 2011) studied PD from generation 2–6 via all-atom molecular dynamic simulations using different force fields and different coarse-graining schemes. Results showed that

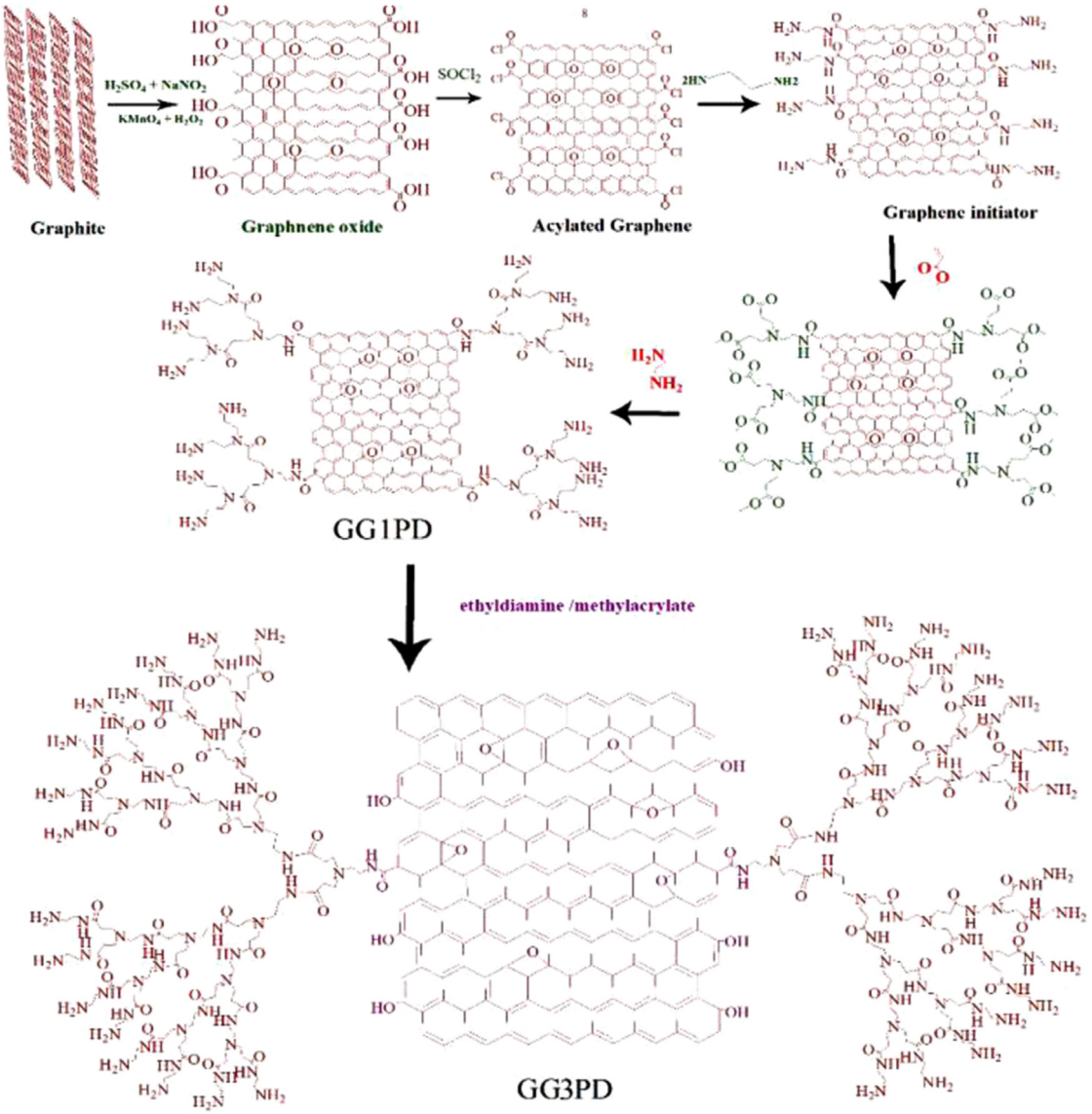

Scheme 1. The schematic procedure for syntheses of GGn ≤ 3PD.

generation 2 and 3 PD had a fractal structure. Well-defined three-fold symmetry patterns in normal-incidence selected area electron diffractions (SAED) were observed for all samples (Fig. S-1a-c), which are similar with that of the liquid exfoliated graphene (Camarada, 2017), demonstrating the increasing crystallinity of Gn ≤ 3PD functionalized rGO. SEM images analysed 2D structures and crumpling features of Gn ≤ 3PD with rGO cores (Fig. 1f-h), as these features have potential advantages in heavy metal ion adsorption and complex functionalization of amine groups on both sides of 2D (Camarada, 2017). The distribution of PD on rGO was evaluated by quantitative energy dispersive X-ray spectroscopy (Fig. 2b). The re-stacking of rGO layers tended to appear on edges of 3D fractal structures of GGn ≤ 3PD (Fig. 1f-h), which can be highly efficient in the dissolution process and can prevent the agglomeration of carbon nanosheets.

Diffraction peaks in the XRD pattern of rGO appeared to be 12.32° (Fig. 2a). Whereas XRD patterns of PD with rGO cores show a typical broad peak with an obvious disappearance of characteristic peaks (Fig. 2a), which might be attributed to very thin rGO layers with a high degree of exfoliation. The diffraction pattern observed at 24.60° for pure graphite carbons from rGO, Fig. 2a was slightly shifted to 0.78, 0.38 and 0.25°, illustrating that PD with rGO cores could be composed of mostly single or few layers. The broadening of Bragg's peaks indicated the formation of crystalline power, and the size was calculated using Equation S-1. Using the full width half maxima (FWHM) of (111) peak, the crystalline nature of rGO in the presence of PD revealed a decrease in the peak intensity and broad peak appearance due to the formation of graphite crystalline fractal nanostructures.

XPS wide spectrum shows that the hybrid film is composed of C, O, and N elements (Fig. 2b). The composition and chemical environment on the surface of composite materials were identified by the amount and oxidation states of elements C and N. The spectra of rGO contain five C 1*s* peaks corresponding to C=C at (284.3 eV), C–OH at (285.7 eV), C–O–C (286.6 eV) and O–C=O at (288.7 eV, Fig. S-2). The O 1*s* band obtained for rGO powder sample shows two peaks at 532.6 and 533.6 eV for the C-OH and COOH groups. The wide scan of Gn ≤ 3PD at 284.5 peak intensity increased for carbon peaks (Fig. 2b, and d-f). However, C 1*s* spectra show that Gn ≤ 3PD perform low binding

energy for the peak at 286.5 due to the C–N coupling, which decreased the p conjugation of systems influenced by the rGO reduction (Fig. 2d-f). Binding energies for different types of carbon are 284.47 eV (graphitic C=C species), 285.3 eV (C-C), 286.25 eV (C-N) and 288.0 eV (N-C=O, Benayad et al., 2009; Retzko and Unger, 2003). Especially the position of the peak intensity at 288.87 eV gradually increased due to the hydrophobicity. An improved peak intensity height was registered

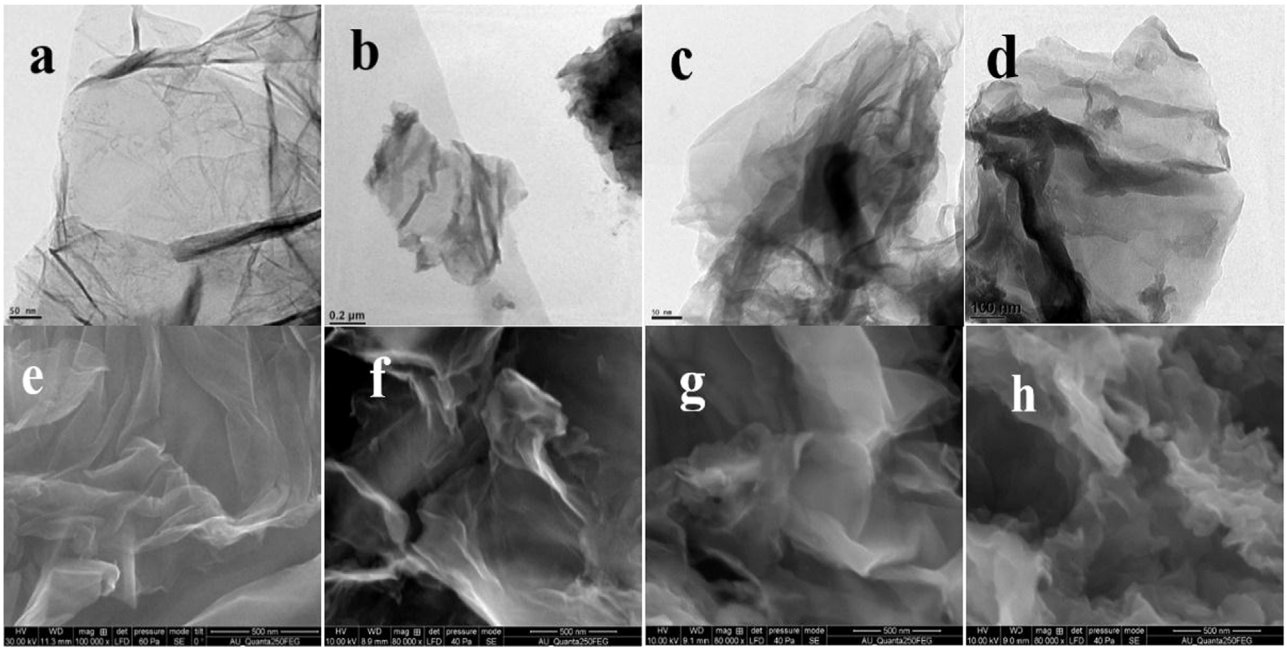

Fig. 1. TEM (a-d) and SEM (e-h) images of GO, GG1PD, GG2PD and GG3PD.

due to the successful functionalization of PD on rGO surface. Binding energy values for the C=C in GG2PD (284.5 eV) are higher than GG3PD (284.8 eV) and lower than GG1PD. The binding energy values of C-O and N-C=O of GG2PD (286.13 eV) are higher compared to the GG1PD (285.04 eV) and GG3PD (285.92 eV, Zharnikov et al., 2000). Meanwhile, the shift may be attributed to the higher resonance structure of N-C=O in the GG2PD, which has a structure with smaller hydrophobic cavities (Uvdal and Viking, 2001). Additionally, N 1*s* region was fitted to the open structure of G1PD and G2PD grafted by three peaks assigned to lower binding energy (located at 399.5 eV). It was attributed to uncharged amine sites (–NH_2), delocalized polar on-type nitrogen –N–(C=O) (400.8 eV) and positively charged protonated amine nitrogen atoms $=N^+(CH_3)_2$ (401.2 eV). The additional peak was assigned to –N = imine nitrogen at the ring (398.5 eV), which can be attributed to the fractal structure of the grafted GG3PD on the rGO surface (Fig. 2g-i). In fact, FT-IR spectroscopy studies on rGO (Fig. 2c) shown broad and intense peaks at 3436, 1734, and 1258 cm^{-1} corresponding to the stretching vibration of O–H, C=O, and C–O groups, respectively. The GG1PD (Fig. 2c) could be confirmed by the appearance of -NH_2 peak at 3435 cm^{-1} and C=O peak at 1722 cm^{-1} (Retzko and Unger, 2003). In the spectra of G2PD-NH_2 and G3PD-NH_2 in presence of rGO, the peaks at 1644 and 1541 cm^{-1} are progressively stronger, probably increased by the internal hydrophobicity, indicating the presence of GG3PD.

3.2. Electrochemical properties of AuNPs/GGn ≤ 3PD

CVs of both GGn ≤ 3PD and AuNPs/GGn ≤ 3PD electrodes exhibited quasi-reversible redox behaviours of $[Fe(CN)_6]^{3-/4-}$ (Fig. 3a and b). peak positions of AuNPs modified or unmodified GG2PD and GG3PD electrodes were shifted towards higher positive potentials relating to the growing up of the fractal structure in comparison with both GG1PD and AuNPs/GG1PD electrodes. The peak-to-peak separation (ΔE_p) between reduction and oxidation peaks of GGn ≤ 3PD increased in an order, and their values were 56 mV, 64 mV, and 73 mV, respectively. $E_{1/2}$ values ($E_{1/2} = E_{pa} + E_{pc}/2$) were 145 mV for GG1PD, 340 mV for GG2PD, and 293 mV for GG3PD. These observations suggested that the charge transfer rate increased with increasing generations of PD although the rGO core was used instead of conventional cores. Since rGO cores were common for all three PD, the increased charge transfer rate or internal hydrophobicity was related to the increased number of -NH_2 of PD. EIS behaviours of all three Gn ≤ 3PD showed the semi-circle and a linear Warburg diffusion line in the high and low frequency regions for GG2PD, while in GG1PD and GG3PD, only the Warburg's diffusion line (Fig. 3c and d). In other words, GG2PD followed the mixed (charge and diffusion) transport kinetic, but GG1PD and GG3PD followed only the diffusion-controlled charge transfer kinetics. The mixed charge transport kinetic of GG2PD was clearly related to the presence of lower branch defects, and thus a more flexible and linear structure, which was in accordance with CV profiles (Fig. 3a and b). However, GG3PD had rigid and fractal or globular structure with larger -NH_2 terminals, which facilitated the interaction with $[Fe(CN)_6]^{3-/4-}$ and resulted in higher current and lower ΔE_p (Fig. 3a and b). The charge density of each structure and its interaction with redox systems were examined by EIS. The increased surface roughness with the increasing generation of PD was indicated by CPE exponent 'n', which exhibited the following order: 0.857 for GG1PD with an open flexible structure < 0.880 for GG2PD with an open fractal structure and < 0.899 for GG3PD with a globular fractal structure. This tendency was related to the increasing cavities towards the hydrophobic nature of PD. The charge transfer resistances (R_{ct}) of GGn ≤ 3PD decreased with the increasing generation of PD (Fig. 3c and d) and followed the reverse order: 4.469×10^3 Ω cm^{-2} (GG1PD) < 4.281×10^3 Ω cm^{-2} (GG2PD) < 5.280×10^2 Ω cm^{-2} (GG3PD) (Table S-1). This was related to the increased number of -NH_2 that enhanced the catalysis of $[Fe(CN)_6]^{3-/4-}$ at the applied DC potential 250 mV. AuNPs were used for the enhancement of Raman behaviours. The behaviours of D, G and 2D bands in SERS were presented for three composites in Fig. 3e and f. All three composites shown four major peaks of D, G, 2D and D + G at 1350, 1607, 2683 and 2911 cm^{-1}, respectively (Ferrari and Robertson, 2000). Generally, all three bands intensities decreased 10-fold for both GG2PD and GG3PD, even in presence of AuNPs. This was revealed by the near constant behaviour of ID/IG ratio (Table S-2), for all three composites. It is worth noting that three values were calculated from the area under respective peaks (Ferrari and Robertson, 2000). The calculated ID/IG ratios for all three GGn ≤ 3PD nanohybrids are 1.04, 1.10 and 0.74 nm, respectively. The ID/IG ratio for the non-functionalized rGO is 1.20. The lower ratios for all GGn ≤ 3PD nanohybrids suggested the efficient functionalization of rGO with PD. Although GG1PD and GG3PD showed similar graphene size, their structural differences (planar or fractal and globular) had greater influence on electronic properties of graphene. The 2D and

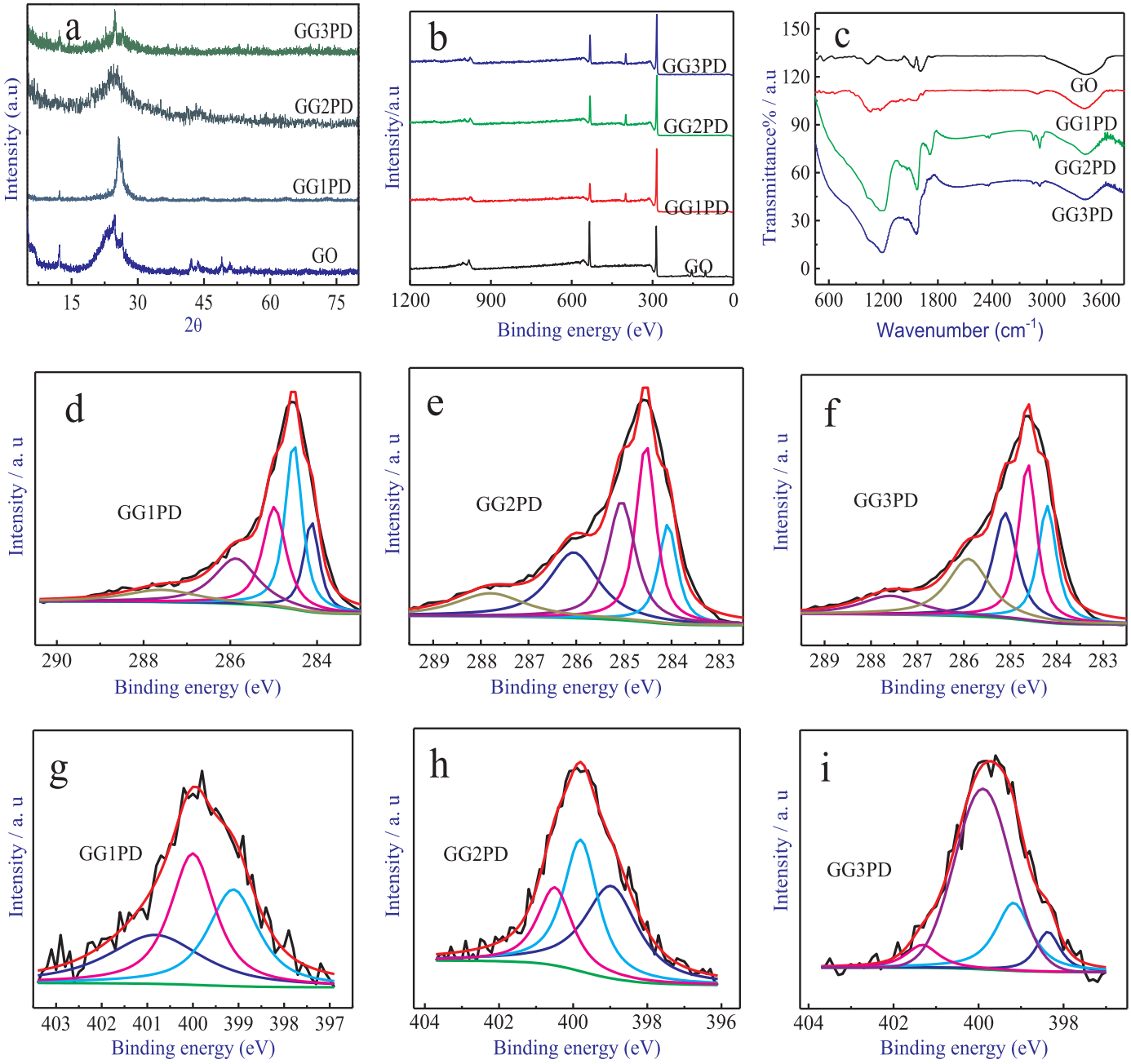

Fig. 2. XRD (a), XPS (b), FTIR (c), C1s XPS (d-f), and N 1s XPS (g-j) spectra of Gn ≤ 3PD.

D + G peak intensities are nearly nullified in presence of AuNPs for all three GGn ≤ 3PD nanocomposites, and their ID/IG ratios were 0.77, 0.74 and 0.77, respectively. These data clearly suggested that GG1PD and GG3PD nanohybrids had similar activities, whereas GG2PD seemed to have different behaviours. The decreased ID/IG ratios were in contradiction with previous reports, where the increased ID/IG ratio for rGO-metal NPs was reported (Ferrari and Robertson, 2000). Thus, decreased ID/IG ratios indicated that the AuNPs content reduced -OH to create new sp2 carbon clusters and enhanced sp3 carbon atoms.

The lowest ID/IG ratio value of 0.77 for GG2PD suggested that hydrophobic cavities were more flexible compared to other two PD nanohybrids. This could be further evidenced by observing the large change in the sp2 carbon crystalline size (from 13.94 to 25.03 nm) calculated using the Equation S-2. The large crystal size indicated the small internal hydrophobicity or planarity and high amount of active AuNPs on the GG2PD surface. This could explain the higher activity of AuNPs/GG2PD in presence of 1 mM $[Fe(CN)_6]^{3-/4-}$ in comparison with other two PD nanohybrids.

AFM images were also described for probe I (Fig. 4a-i). The attachment of GGn ≤ 3PD was indicated clearly by the formation of a densely packed platelet like film on MPA (Fig. 4a-c). GG2PD exhibited a porous structure and an increased surface height from 35.16 to 70.1 nm, showing that the fractal structure was flexible and depended on the internal hydrophobicity and charge density. In the case of GG3PD, the height of the profile decreased to 15.4 nm, indicating uniform fractal nano-structural morphology. The functionalization of PD with AuNPs smoothened the film and decreased the porosity nature, which was in accordance with CV results, showing decreased redox behaviours of $[Fe(CN)_6]^{3-/4-}$ for AuNPs/GGn ≤ 3PD films (Fig. 3d). However, the average surface height of AuNPs/GGn ≤ 3PD decreased to homogeneous package of AuNPs on surface with values of 17.69 nm, 37.12 nm and 35 nm, respectively (Fig. 4a-c), indicating the uniform

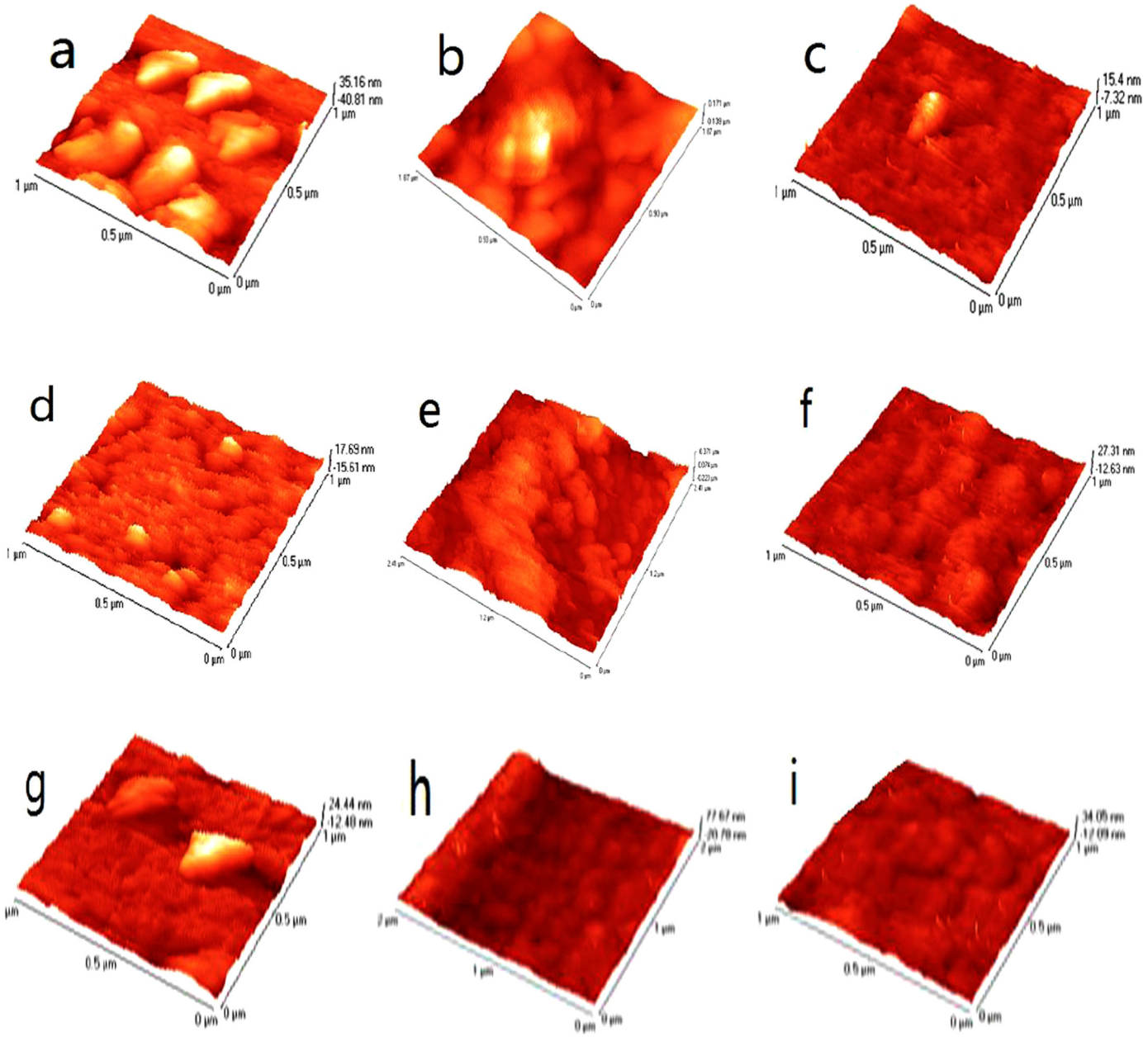

Fig. 3. AFM images of (a) GG1PD, (b) GG2PD, (c) GG3PD, (d) AuNPs/GG1PD, (e) AuNPs/GG2PD, (f) AuNPs/GG3PD, (g) ssDNA/AuNPs/GG1PD, (h) ssDNA/AuNPs/GG2PD, and (i) ssDNA/AuNPs/GG3PD modified MPA/Au electrode.

deposition of AuNPs over GGn ≤ 3PD films.

The size of internal cavities in GG3PD was probably higher than that in GG2PD. The hydrophilic groups such as hydroxide, epoxide, carbonyl, and amide groups of rGO functionalized Gn ≤ 3PD on both sides of basal planes of rGO could generate a flexible 3D nanostructure of AuNPs composite films. EIS showed higher R_{ct} values following the deposition of AuNPs on the GGn ≤ 3PD surface in comparison with CVs (Fig. 3a-d). R_{ct} values of each AuNPs/GGn ≤ 3PD electrodes presented following orders: 1.16×10^4 Ω cm^{-2}, 7.788×10^3 Ω cm^{-2}, 4.780×10^3 Ω cm^{-2}. AuNPs/GG1PD showed one order increased R_{ct} related to its high ability to control charge transfer kinetics (Fig. 3c and d). AuNPs/GG2PD and AuNPs/GG3PD showed higher charge capacitances and surface coverages because of minimal defects, which is consistent with R_{ct} of GG2PD and GG3PD (Fig. 3c and d). As previously reported, the hydrophobic character of the ethylene core was improved by using elongated methylene core to increase host-guest interactions in presence of hydrophobic dye such as nile red (Newkome and Shreiner, 2008).

Hence, the globular structure of GG3PD might force the charge transfer to dominate the diffusion process. Diffusion coefficients (*D*) of GGn ≤ 3PD electrode were calculated from plots of peak currents *vs.* the square root of scan rates, following the Randles-Sevcik equation (Equation S-3). The D value of the bare Au electrode was 1.2×10^{-5} cm^2 s^{-1}, while the D value of MPA/Au electrode decreased to 4.472×10^{-6} cm^2 s^{-1}(Fig. S-4), indicating that MPA had a blocking effect towards $[Fe(CN)_6]^{3-/4-}$ as the redox probe. D values of GGn ≤ 3PD/MPA/Au electrode were 3.7×10^{-5}, 6.39×10^{-4} and 6.31×10^{-7} cm^2 s^{-1}, respectively (Fig. S-4). GG1PD/MPA/Au electrode showed the highest D value (3.7×10^{-5} cm^2 s^{-1}), which was close to the MPA/Au electrode. GG2PD/MPA/Au electrode showed higher D value than GG3PD/MPA/Au electrode, which is related to the exposed hydrophobic structural defects on the higher generation that can easily generate the charge density of PD for ferricyanide interaction on rGO. Since hydrophobic character increased with the increasing

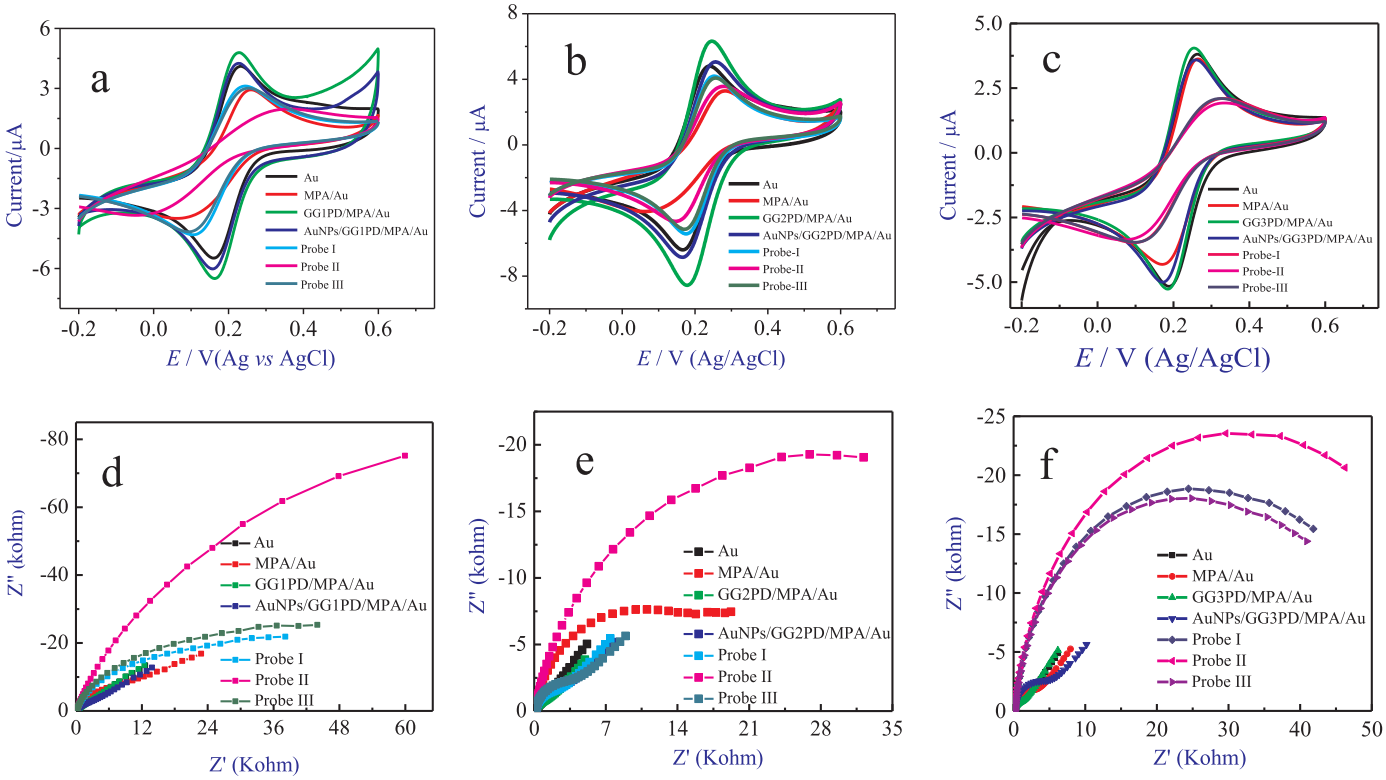

Fig. 4. CV (a-c) and EIS (d-f) of different electrodes.

generation of PD, more repulsion was exerted by GG3PD along with its fractal structure. The large D value for GG2PD/MPA/Au electrode again indicated the maximized interaction with ferricyanide because of the planner, open or fractal structure.

3.3. AuNPs/Gn≤3PD for DNA nanobiosensing

The ssDNA was successfully linked onto the surface of AuNPs/GGn≤3PD/MPA/Au electrode to form probe I, which resulted in increasing both ΔE_p (Fig. 4a-c) and R_{ct} (Fig. 4e-f) and decreasing peak currents (Fig. 4a-c) because of the electrostatic repulsion between the negative charge of phosphate backbones of ssDNA and redox probe $[Fe(CN)_6]^{3-/4-}$ and the introduction of non-conducting ssDNA. The cDNA could successfully hybridize with probe I to form probe II, which further enlarged both ΔE_p (Fig. 4a-c) and R_{ct} (Fig. 4e-f) and decreased peak currents (Fig. 4a-c), indicating further increase in the non-electroconductivity of dsDNA and enhancement in the electrostatic repulsion between negative charges of phosphate backbone of dsDNA and $[Fe(CN)_6]^{3-/4-}$. However, the ncDNA might hybridize with probe I, which formed probe III and led to negligible changes in peak currents (Fig. 4a-c), ΔE_p (Fig. 4e and f), and R_{ct} (Fig. 4a-c), suggesting excellent selectivity of the fabricated DNA nanobiosensor (Table S-3).

AFM images of ssDNA/AuNPs/GGn≤3PD/MPA/Au electrode (Fig. 3g-i) indicated that the surface became rougher, and the average surface height has increased from 17.69, 71.01 and 27.31 nm to 24.44, 77.01 and 34.65 nm because of the nonspecific adsorption of ssDNA. In contrast, the decrease of the surface roughness and the increase of the hydrophobic cavities size reduce the blocked effect owning to the formation of 3D fractal nanostructure of GGn≤3PD, which could increase the homogeneity of the adsorption of the capture probe DNA molecules. Obviously, probe DNA molecules contributed with reliable 3D fractal nanostructures, which improved DNA hybridization.

ΔR_{ct} (the difference for R_{ct} between probe I and probe II) values of three GGn≤3PD-based probe were calculated on basis of internal cavities and flexible structure. Their values were 0.78 W cm^{-2} for GG1PD-based probe, 1.80 W cm^{-2} for GG2PD-based probe, and 1.00 W cm^{-2} for GG3PD-based probe, respectively (Fig. 4d-f), indicating that the GG2PD-based probe was more sensitive than other two probes because of their flexible and hydrophobic cavities (Fig. 4d-f).

A regular decrease in the impedance (Fig. 5a-c) with decreasing target DNA concentrations was noticed for GGn≤3PD-based probe. The changes in ΔR_{ct} were plotted against logarithmic DNA concentrations (log C_{DNA}). The linear increase of ΔR_{ct} with the increasing log C_{DNA} was presented in Fig. 5d-f. DNA nanobiosensors shown wide linear ranges from 1×10^{-6} to 1×10^{-13} M for GG1PD-based probe with low LOD of 3.34×10^{-14} ;M, 1×10^{-6} to 1×10^{-18} M for GG2PD-based probe with low LOD of 1.87×10^{-19} M, and 1×10^{-6} to 1×10^{-15} M for GG3PD-based probe with low LOD of 3.87×10^{-16} M. According to their slopes, we could infer that their sensitivities were 1.19 KΩ M^{-1} for GG1PD-based probe, 2.37 KΩ M^{-1} for GG2PD-based probe and 1.07 KΩ M^{-1} for GG3PD-based probe. Jimenez-Ruiz et al. reported that the highly stable dendritic structure of AuNPs/GGn≤ 3PD enhanced catalytic activity and decreased LOD. AuNPs functionalized GG1PD and GG2PD presented more stable dendritic open fractal structure, while AuNPs/GG3PD exhibited an intermediated structure with globular or open fractal configuration (Jimenez-Ruiz et al., 2017). In addition, DPV (Fig. S-4) can also detect changes of DNA concentrations in presence of methylene blue (MB) that has strong affinity for dsDNA than ssDNA, indicating that DPV can replace EIS to realize the fast determination of DNA hybridization. In comparison with electrochemical genosensors based on PD nanocomposites in previous reports (Table S-4), the presented DNA nanobiosensors based on GG2PD-based probe I had the widest linear range and lowest LOD, implied that the proposed DNA nanobiosensor as a potential electrochemical biosensing platform can apply for genosensing in different fields.

The selectivity of DNA nanobiosensors based on GGn≤3PD-based probe was further evaluated by monitoring changes in R_{ct} (Fig. 5g-i). A three-time decrease of ΔR_{ct} was noticed compared to the probe III interaction, confirming efficient selectivity towards the sequence specificity. The high selectivity could also be related to high surface area in

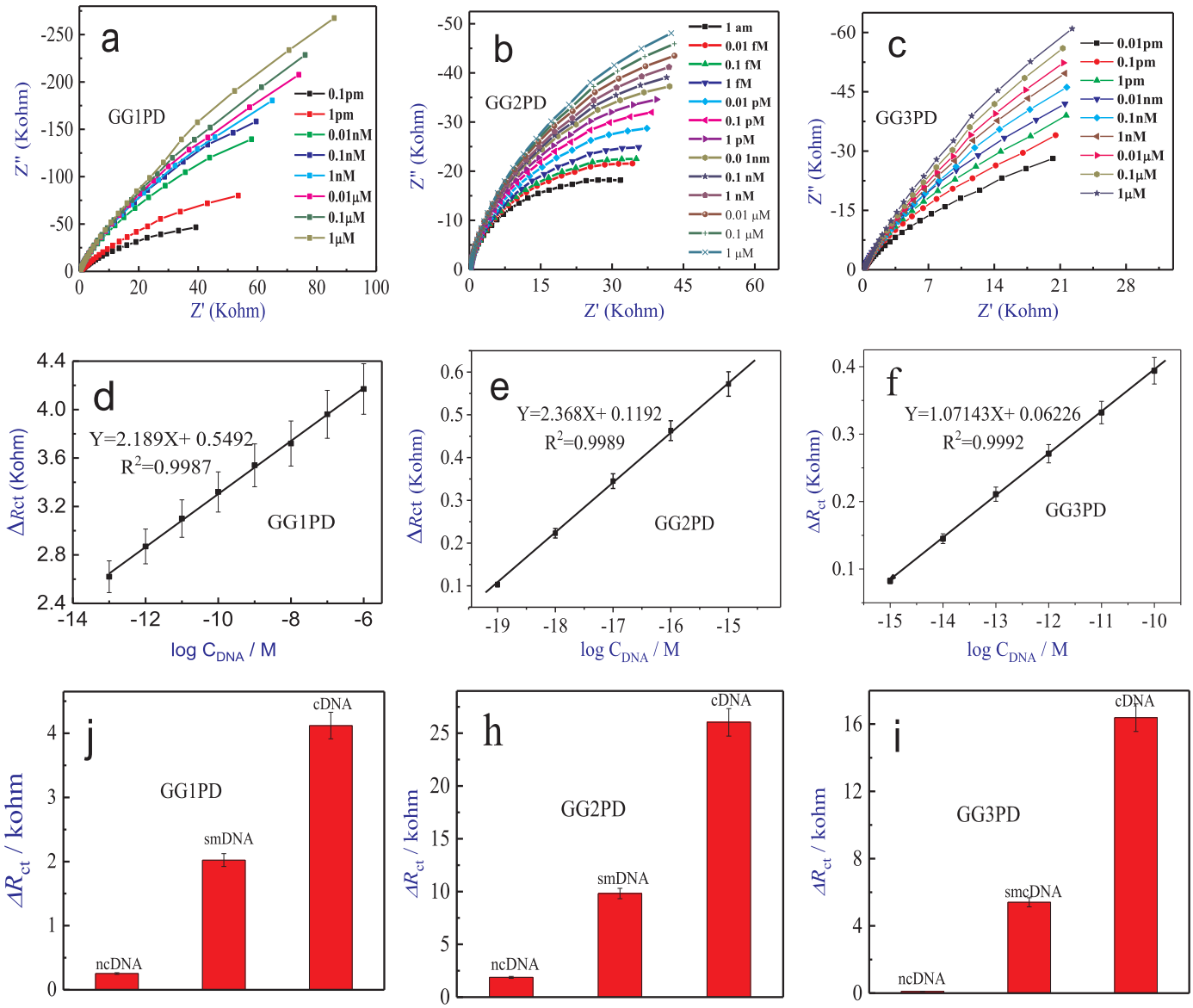

Fig. 5. EIS (a-c), the linear relationship (d-f), and selectivity (j-i) of GGn≤3PD-based probe.

the presence of AuNPs that provide larger binding sites for immobilizing larger number of ssDNA.

4. Conclusions

A novel electrochemical gene nanobiosensor based on a 3D fractal architectural nanohybrid of AuNPs/GGn≤3PD for rapid, sensitive, and ultra-trace detection of label-free DNA hybridization was successfully developed. Gn≤3PD with rGO as cores displayed a high fractal nanoarchitecture and more flexible structure, which improved elelctrocatalytic activity, increased specific surface area, and enhanced gene biosensing performance. AuNPs encapsulated onto the highly-stable 3D fractal nanostructure surface of GGn≤3PD controlled the particle size of AuNPs, showed strong physical interaction and efficient binding to hydroxyl groups of rGO, healed two dimensional crumpled structures, and produced conducting effect, which displayed fast electron charge transfer properties, large specific surface area, high electrical conductivity, improved structural defect and stability, high electrocatalytic activity, excellent mechanical stability, high-ultra sensitivity and specificity against gene biosensing. In comparison with GG1PD-based and GG3PD-based probe, GG2PD-based probe with the fractal open structure had higher value of the heterogeneous electron transfer, better structural stability, the lowest mobility on solid surface with the increasing charge resistance, widest linear ranges and lowest limit of detection. This will provide a new candidate for the development of metal nanoparticles functionalized PD with inorganic nonmetallic nanomaterials as cores with 3D fractal nanoarchitecture and promising electrochemical DNA nanobiosensing platforms based on dendrimer-nanoinorganic hybrids with 3D nanoarchitectures and LBL assembly for fast and ultra-trace detection of label-free DNA hybridization.

Acknowledgements

This work was supported by CSIR (03(1160)/10/EMR-II), and DST INSPIRE (04/2015/000337), Govt. of India and Fondecyt Chile Project Regular (1180023), Supercomputing infrastructure of NLHPC (ECM-02), Outstanding Young Talent Program in Jiangxi Province (20171BCB23042), and NSFC (51662014).

Appendix A. Supporting information

Supplementary data associated with this article can be found in the

online version at doi:10.1016/j.bios.2018.08.032.

References

Aixue, L., Yang, F., Ma, Y., Yang, X., 2007. Biosens. Bioelectron. 22, 1716–1722.
Bromfield, S.M., Posocco, P., Fermeglia, M., 2016. Talanta 148, 427–438.
Brunetti, V., Boucheta, L.M., Strumia, M.C., 2015. Nanoscale 7, 3808–3816.
Benayad, A., Shin, H.J., Lee, Y.H., 2009. Chem. Phys. Lett. 475, 91–95.
Chen, A., Chatterjee, S., 2013. Chem. Soc. Rev. 42, 5425–5438.
Chen, D., Feng, H.B., Li, J.H., 2012. Chem. Rev. 112, 6027–6053.
Camarada, M.B., 2017. J. Phys. Chem. A 121, 8124–8135.
Guo, S., Wang, E., 2011. Nano Today 3, 240–264.
Jayakumar, K., Camarada, M.B., Dharuman, V., Ju, H.X., Dey, R.S., Wen, Y.P., 2018a. Nanoscale 10, 1196–1206.
Jayakumar, K., Camarada, M.B., Dharuman, V., Rajesh, R., Venkatesan, R., Ju, H.X., Maniraj, M., Rai, A., Barman, S.R., Wen, Y.P., 2018b. Appl. Mater. Interfaces 10, 21541–21555.
Jimenez-Ruiz, A., Carnerero, J.M., Castillo, P.M., Prado-Gotor, R., J., 2017. J. Nanopart. Res. 19 (24-24).
Kumar, N.A., Choi, H.J., Shin, Y.R., Chang, D.W., Dai, L., Baek, J.B., 2012. ACS Nano 6, 1715–1723.
Kleinman, M.H., Flory, J.H., Tomalia, D.A., Turro, N.J.J., 2000. Phys. Chem. B 104, 11472–11479.
Li, F., Peng, J., Zheng, Q., Guo, X., Tang, H., Yao, S., 2015. Anal. Chem. 87, 4806–4813.
Lei, J., Ju, H.X., 2012. Chem. Soc. Rev. 41, 2122–2134.
Liu, J., Liu, J., Yang, L., Chen, X., Zhang, M., Meng, F., Luo, T., Li, M., 2009. Sensors 9, 7343–7364.
Newkome, G.R., Shreiner, C.D., 2008. Polymer 49, 1–173.
Rao Vusa, C.S., Manju, V., Berchmans, S., Arumugam, P., 2016. RSC Adv. 6, 33409–33418.
Rahman, K.M.A., Durning, C.J., Turro, N.J., Tomalia, D.A., 2000. Langmuir 16, 10154–10160.
Retzko, I., Unger, W.E.S., 2003. Adv. Eng. Mater. 5, 519–522.
Sang, S., Wang, Y., Feng, Q., Wei, Y., Ji, J., Zhang, W., 2016. Crit. Rev. Biotechnol. 36, 465–481.
Trinchi, A., Muster, T.H., 2007. Supramol. Chem. 19, 431–445.
Uvdal, K., Viking, T.P., 2001. Langmuir 17, 5324–5328.
Xu, X., Ran, Q., Haag, R., Ballauff, M., Dzubiella, J., 2017. Macromolecules 50, 4759–4769.
Zhou, X., Tyson, D.S., Castellano, F.N., 2000. Angew. Chem. Int. Ed. 39, 4301–4305.
Zhong, T., Ai, P., Zhou, J., 2011. Fluid Phase Equilibr. 302, 43–47.
Zharnikov, M., Frey, S., Heister, K., Grunze, M., 2000. Langmuir 1, 2697–2705.